

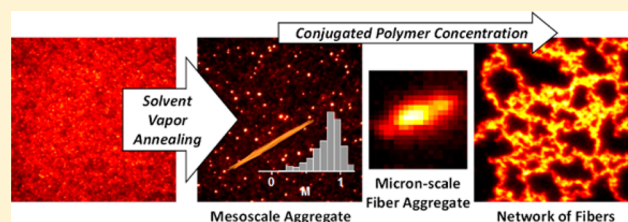
Highly Anisotropic Conjugated Polymer Aggregates: Preparation and Quantification of Physical and Optical Anisotropy

Jaesung Yang, Heungman Park,[†] and Laura J. Kaufman*[‡]

Department of Chemistry, Columbia University, New York, New York 10027, United States

Supporting Information

ABSTRACT: Controlling morphological order of conjugated polymers over mesoscopic and microscopic scales could yield critical improvements in the performance of organic electronics. Here, we utilize a multimodal apparatus allowing for controlled solvent vapor annealing and simultaneous wide-field epifluorescence microscopy to demonstrate bottom-up growth of morphologically ordered anisotropic aggregates prepared from single poly(2-methoxy-5-(2-ethylhexyloxy)-1,4-phenylenevinylene) (MEH-PPV) chains, with length scales controllable from tens of nanometers to several micrometers. Preparation of micrometer-scale fiber aggregates that interconnect to form spanning networks is also demonstrated. We quantify aggregate physical and optical anisotropy, degree of quenching, and exciton diffusion characteristics as a function of aggregate size. The demonstration of controlled preparation of highly anisotropic aggregates provides a path for controlled postprocessing of organic thin films at length scales relevant to the operation of devices.



INTRODUCTION

Traditionally, it has been believed that achieving high efficiency in organic semiconductors requires crystalline morphology and long length scale order. Recent reports, however, show that interconnection of conjugated polymer aggregates with mesoscopic order may lead to efficient charge carrier transport on device length scales,^{1–3} transport that in turn can lead to high efficiency in seemingly disordered organic semiconductor based devices.^{4–7} These reports highlight the importance of morphological control of conjugated polymer assemblies over a variety of length scales, from the mesoscopic level. Achieving such control has proven challenging, as mesoscopic and larger structures originate from self-assembly of many single polymer chains. These single chains themselves display a high degree of complexity in conformation and interactions that are not fully understood,⁸ and the self-assembly of these polymers introduces additional complexity, as the conditions under which aggregates are prepared affect chain density and organization that in turn affect aggregate photophysics.

In the active layers of bulk heterojunction devices, formation of mesoscopically ordered aggregates and their interconnection into percolated networks rely largely on molecular design and solution processing conditions.^{3,9,10} To achieve a higher degree of control of aggregate morphology, bottom-up approaches have been attempted, though the resulting aggregates have not typically shown a high degree of mesoscopic order.^{11–19} Recently, aggregates prepared via solvent vapor annealing (SVA) of poly(2-methoxy-5-(2-ethylhexyloxy)-1,4-phenylenevinylene) (MEH-PPV)/host polymer blended films were demonstrated.¹¹ Small aggregates of ~20 single chains prepared via this approach exhibited a high degree of morphological order, but at increasing size a loss of ordering was seen.¹¹ To

determine the number of chains per aggregate, previous studies relied on a counting approach that requires dilute concentrations in which fluorescent features are well-isolated.^{11–14} This prerequisite limited growth of larger aggregates, desirable for potential long-range charge carrier transport, owing to the relative paucity of building block single chains for self-assembly.

The limited ordering in the larger aggregates prepared in previous studies may be overcome by enhanced control over the solvent vapor swelling used to prepare such aggregates. Processing parameters include choice of solvent, pressure and flow of solvent vapor as well as degree and time of film swelling. These parameters indeed have strong impacts on the final morphology and properties of organic thin films.^{20,21} Recently, we developed a multimodal apparatus that allows precise control of solvent vapor delivery and wide-field fluorescence imaging during and following SVA.²² Using this system, here we demonstrate control of morphological order of MEH-PPV aggregates over a wide range of length scales by tuning initial MEH-PPV concentration in polymer blended thin films. We introduce intensity analysis designed for use in concentrated films that, when combined with complementary analyses, allows for quantitative assessment of fundamental aggregate physical and photophysical attributes. In particular, we show that aggregates consisting of from ~50 to 1000 single MEH-PPV chains exhibit a high degree of physical and optical anisotropy, indicating a high degree of internal ordering that supports exciton migration. This finding is buttressed by the finding that these aggregates display discrete changes in intensity, with

Received: March 9, 2017

Revised: May 9, 2017

Published: May 31, 2017

extent of change increasing with physical size, demonstrating efficient exciton diffusion at mesoscopic length scales. More generally, this work provides an approach to preparing and assessing mesoscopic materials composed of conjugated polymers over a wide range of length scales, toward tailoring structure and function of organic electronics.

EXPERIMENTAL METHODS

Sample Preparation. MEH-PPV was synthesized as described previously.²³ The MEH-PPV had $M_w = 168$ kDa with PDI = 2.1, with a single-peak trace measured by gel-permeation chromatography. Poly(methyl methacrylate) (PMMA; $M_w = 97$ kDa and PDI = 2.2) was purchased from Sigma-Aldrich. Sample films were prepared by spin-casting a toluene solution of MEH-PPV containing 6.0 wt % PMMA on a quartz crystal microbalance (QCM) sensor and a glass coverslip at ~ 2800 rpm to yield film thickness of 280 ± 5 nm, as measured by the QCM-mounted film (Supplementary Text 1). Films of four MEH-PPV concentrations were prepared, which will be denoted concentrations A, B, C, and D. Sample films prepared at concentration A (300 fM) exhibited isolated fluorescent features at a density of ~ 0.6 spots/ μm^2 . MEH-PPV concentration was increased by 10, 100, and 1000 times, respectively, to create films of concentrations B–D (3, 30, and 300 pM, respectively).

Solvent Vapor Delivery and Control. Details of the experimental apparatus are provided elsewhere.²² Briefly, the system consists of a mass flow controller (MFC; Alicat Scientific, MCS-200SCCM) based solvent vapor control system, a QCM (Stanford Research Systems, QCM-200) for assessment of film swelling, and a wide-field fluorescence imaging system. The solvent vapor control system was configured with two channels, where MFCs in each channel allowed direct, quantitative control of volumetric flow rate, Q_{nit} , of dry nitrogen carrier gas and solvent vapor generated from gas bubbling. One channel was used to bubble the carrier gas through a solvent reservoir with an acetone–chloroform liquid solvent mixture and generate solvent vapor. This flowed into a mixing bottle to ensure a reservoir of equilibrated vapor and then was directed toward a sample chamber. This flow channel had a switch, which allowed the carrier gas to flow toward the mixing bottle by bypassing the solvent reservoir. The other channel was configured such that the carrier gas directly flowed toward the mixing bottle. With this configuration, Q_{nit} could be maximized when drying as-cast films and deswelling films.

Solvent Vapor Annealing. The QCM- and coverslip-mounted sample films were placed at the lid and base, respectively, of the custom-built sample chamber and exposed to dry nitrogen gas flow at $Q_{\text{nit}} = 400$ sccm (cm^3/min) for 60 min to remove residual solvents. The films were swollen with solvent vapor using an acetone–chloroform solvent mixture with liquid volume ratio of 50:50%. This liquid volume ratio led to a vapor volume ratio of 56.3:43.7%, as calculated from the liquid–vapor equilibrium curve for acetone–chloroform liquid solvent mixtures. Initial Q_{nit} for film swelling was 170 sccm, which was decreased progressively to ~ 40 sccm after the film was fully swollen to maintain the plateau thickness. Film thickness in the plateau period and film to film variation was strictly held to be within ± 5 nm to ensure well-controlled, reproducible aggregate preparation. Unless otherwise mentioned, films were swollen for 50 min, after which films were deswelled by the flow of dry nitrogen gas ($Q_{\text{nit}} = 400$ sccm). The N_2 gas flow continued while subsequent fluorescence-

based experiments were performed. In all experiments, temperature was held at 21 °C.

Wide-Field Epifluorescence Imaging. For excitation, 488 nm light from a continuous-wave diode laser (Thorlabs, L488P60) was used. The laser beam was coupled into a multimode fiber, which was shaken mechanically to eliminate speckles and homogeneously illuminate the field of view (FOV), which was $47 \mu\text{m} \times 47 \mu\text{m}$. Circularly polarized light was produced by a quarter wave plate, passed through a laser line filter, collimating lens, and removable motorized rotating linear polarizer, and focused onto the back-focal plane of an oil immersion objective (Olympus PlanApo N 60 \times , NA = 1.45) via a dichroic beam splitter to achieve wide-field illumination. Fluorescence was collected by the same objective, spectrally filtered with 514 nm long pass and 520–680 band-pass filters, and imaged onto an EMCCD camera (Andor, iXon DV885 KCS-VP). All images were 16 bits and were recorded over 512 pixels \times 512 pixels.

Fluorescence Intensity Measurements. To attain fluorescence images and compare fluorescence intensity between single MEH-PPV chains and aggregates, 20-frame movies were recorded with exposure time of 100 ms per frame. Then, all frames in each movie were averaged to generate a fluorescence image to average over changes in fluorescence intensity that may occur while recording movies. To minimize influence of photoinduced fluorescence quenching,²⁴ the illumination intensity was chosen to be as low as possible and was $5 \text{ W}/\text{cm}^2$ at the sample, below which we could not adequately determine the single chain fluorescence intensity. At this illumination intensity, fluorescence emission from aggregates prepared from films of concentration D typically exceeded the upper limit of the EMCCD camera; thus, a neutral density filter was placed in the fluorescence detection path, and the fluorescence intensity of these aggregates was corrected later in the analysis.

Fluorescence intensity calculations were performed using a custom computer program written in Python. In this program, fluorescent features, single MEH-PPV chains and aggregates, were identified by the Crocker–Grier algorithm.²⁵ For aggregates, fluorescence intensity, I_{AGG} , was calculated by subtracting the contribution from single MEH-PPV chains coexisting within the diffraction limited spot size as well as camera noise:

$$I_{\text{AGG}} \text{ (or } I_{\text{SM}}) = \sum_{X=1}^N \sum_{Y=1}^N I_{P,XY} - N^2 I_{P,\text{film-median}} \quad (1)$$

N is the number of pixels over which the feature size is defined, $I_{P,XY}$ is pixel intensity within the feature, and $I_{P,\text{film-median}}$ is the median pixel intensity of the fluorescence image, which represents the sum of signal due to fluorescence of remaining dispersed MEH-PPV chains and camera noise. For these calculations, we chose $N = 11$, which includes the zero-order diffraction spot (the Airy disk) and the first diffraction ring (Supplementary Text 2). The fluorescence intensity of single MEH-PPV chains, I_{SM} , which is relevant for films of concentration A before and after SVA, is also calculated via the above equation, and here $I_{P,\text{film-median}}$ is due only to camera noise.

Polarization Anisotropy Measurements. Following fluorescence intensity measurements, a motorized rotating linear polarizer was placed in the excitation laser beam path. The polarization anisotropy measurements were performed by

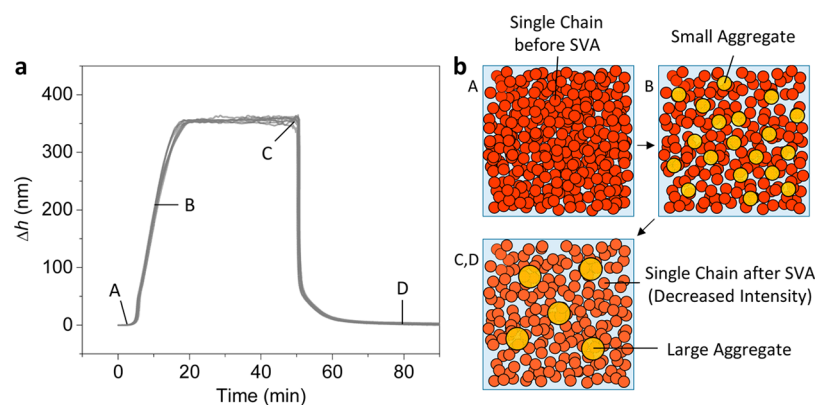


Figure 1. Controlled solvent vapor swelling of conjugated polymer/host polymer films. (a) Change in film thickness (Δh) over time for sample films on the QCM sensor swollen with an acetone–chloroform solvent mixture with vapor volume ratio of 56.3:43.7% (liquid volume ratio of 50:50%). Eight film swelling curves obtained from SVA of two sample films for each concentration, A–D, are overlaid, demonstrating the high degree of reproducibility of the procedure. During and following SVA, corresponding sample films on the glass coverslip were used for wide-field fluorescence imaging. (b) Schematic illustration depicting the growth of MEH-PPV aggregates over the course of the SVA process.

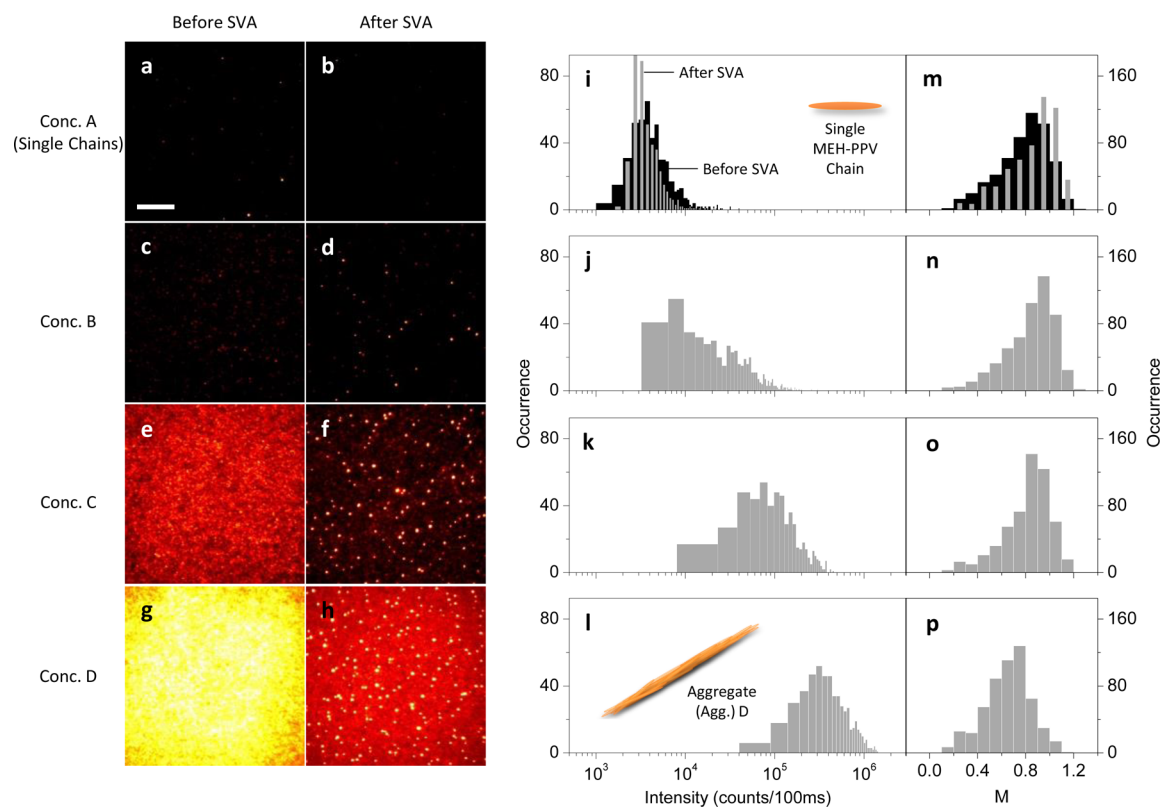


Figure 2. Formation, size, and optical anisotropy of mesoscopic aggregates as a function of conjugated polymer concentration. (a–h) Wide-field fluorescence images of films of concentrations A–D (a, c, e, g) before and (b, d, f, h) after SVA. Intensity scale for the images differs depending on the concentration: 1100–1500, 1100–4000, and 1100–12000 counts per 100 ms for films of concentrations A, B and C, and D. Scale bar is 10 μm . (i–p) Histograms of (i–l) fluorescence intensity and (m–p) polarization modulation depth (M) of single molecules (A) or aggregates (B–D). The intensity histograms are depicted on a semilogarithmic scale. In panels i–l, the median intensities are 4600, 3500, 31000, 111500, and 425100 counts per 100 ms, respectively, for single MEH-PPV chains before and after SVA and aggregates prepared in films of concentrations B–D. In m–p, the median values are $M = 0.82, 0.91, 0.88, 0.85,$ and $0.67,$ respectively, for single chains before and after SVA and aggregates prepared in films of concentrations B–D. Illumination intensity of 5.0 W/cm^2 was used for fluorescence intensity measurements, whereas illumination intensity for the M measurements was set to 40.0, 2.0, 0.7, and 0.2 W/cm^2 for films of concentrations A–D, respectively. At least 500 features obtained from 8–12 fluorescence images collected over two sample films were analyzed for each concentration.

rotating the polarization of linearly polarized excitation light and monitoring fluorescence intensity as a function of polarization angle. The rotation rate was $10^\circ/\text{s}$. The illumination intensity varied depending on fluorescence intensities of single MEH-PPV chains and aggregates, with

power density set to 40.0, 2.0, 0.7, and 0.2 W/cm^2 for features in films of concentration A–D, respectively. The intensity variation was $\pm 3\%$ as a function of polarization angle, primarily due to imperfect optics alignment. The polarization modulation (M) is expressed as $I(\phi) = I_0[1 + M \cos\{2(\phi - \phi_0)\}]$, with

$I(\phi)$ fluorescence intensity as a function of ϕ , the angle of the excitation polarization. I_0 is average fluorescence emission intensity, and ϕ_0 is a reference polarization angle corresponding to the maximum intensity. M values were extracted from fitting the angle-dependent intensity using a custom computer program written in Python. Data analysis was performed as described in ref 26. A single polymer chain or an aggregate thereof with highly aligned absorbing chromophores will show an M value close to 1, while a random arrangement of absorbing chromophores will yield M close to 0.

Fluorescence Intensity Transients. To accelerate photo-bleaching, high illumination intensity (200 W/cm^2) was used. For the measurements of aggregates, neutral density filters with varying transmittance were placed in the fluorescence detection path, and resulting intensity transients were corrected later in the analysis. To assess fluorescence intensity jump size, a step transition and state identification algorithm was employed,²⁷ and analysis was performed using a custom computer program written in Python.

Single Aggregate Diffusion Tracking. To track motion of aggregates in swollen films, 100-frame movies with exposure time of 100 ms per frame were recorded prior to film deswelling. Particle positions were determined and 2D single aggregate trajectories were generated using the ParticleTracker plugin for the ImageJ software. Trajectories >80 consecutive frames in length were used to compute mean square displacements (MSDs) via $\langle \Delta r^2(\tau) \rangle = \langle [r(t + \tau) - r(t)]^2 \rangle$, where τ is the lag time and r is the feature position. The diffusion coefficient, D , was calculated via $\langle \Delta r^2(\tau) \rangle = 2dD\tau + \epsilon$, with $d = 3$, the dimensionality of diffusion. The MSD and subsequent D calculations were performed using a custom computer program written in Igor.

RESULTS AND DISCUSSION

Controlled Film Swelling and Aggregate Formation with Varying Conjugated Polymer Concentration. To prepare mesoscopic aggregates of different sizes, four initial concentrations, which will be denoted concentrations A–D, of MEH-PPV in a host PMMA matrix were used. Sample films prepared at concentration A (300 fM) exhibited isolated fluorescent features at a density of $\sim 0.6 \text{ spots}/\mu\text{m}^3$. Initial MEH-PPV concentration was increased by 10, 100, and 1000 times to create films of concentrations B–D, respectively. In all cases, two MEH-PPV/PMMA blended films were prepared, one on a QCM sensor and one on a glass coverslip. Both were placed in the SVA/imaging sample chamber (see [Experimental Methods](#)). For solvent vapor swelling of the films, an acetone–chloroform solvent vapor mixture with volume ratio of 56.3:43.7% was used. This mixture of solvents enables supersaturation of MEH-PPV to be achieved such that aggregation and Ostwald ripening may be initiated.^{11,28} As-cast films had thickness of $280 \pm 5 \text{ nm}$, which increased by $\sim 350 \text{ nm}$ when the films were swollen to a plateau thickness, as assessed by the change in QCM resonance frequency ([Figure 1a](#) and [Supplementary Text 1](#)). In all cases, films were swollen for 50 min and then deswelled by the flow of dry nitrogen gas.

[Figure 2a–h](#) shows typical fluorescence images obtained from coverslip-mounted films of concentrations A–D before and after SVA. For concentration A, little difference in the number of fluorescent features before and after SVA was evident, indicating that aggregation was not initiated at this low concentration and the fluorescent features represent single isolated chains. As-cast, films of concentration B exhibited a

high density of features in the fluorescence image while films of concentrations C and D exhibited moderate, largely homogeneous fluorescence across the imaging area, consistent with the expectation of multiple fluorophores within each diffraction limited spot. Pixel intensity distributions for the fluorescence images of the as-cast films of concentrations B–D shown in [Figure 2](#) revealed nearly linear increase of overall intensity with increasing concentration ([Supplementary Text 3](#)). This suggests that little fluorescence quenching of single chains is occurring due to increasing concentration and also suggests that the as-cast films are composed primarily of individual chains as opposed to small aggregated species. Swelling these films with acetone–chloroform solvent vapor mixture allowed single chain diffusion and initiated the aggregation process, resulting in the emergence of distinct bright fluorescent features $\sim 10 \text{ min}$ into swelling ([Figure 1b](#) and [Supplementary Movie S1](#)). Aggregate growth continued during the entire time the film was swollen, as evidenced by the increasing brightness, decreasing number, and decreasing diffusivity of the fluorescent features ([Supplementary Movies S2](#) and [3](#)). The final dried films contained a mixture of aggregates and single MEH-PPV chains, with the single chains resulting in high background fluorescence at the higher concentrations explored ([Figure 2f,h](#)).

Fluorescence Intensity and Polarization Anisotropy of Aggregates. We compared fluorescence intensity between single MEH-PPV chains and aggregates prepared in films of concentrations B–D, hereafter referred to as aggregates B–D. Since films containing aggregates also contain single chains remaining after SVA, fluorescence intensity measured from a diffraction limited spot including an aggregate includes fluorescence from not only the aggregate under assessment but also single chains coexisting within the diffraction limited feature size. This single chain contribution, as well as camera noise, was subtracted before determining aggregate fluorescence intensity (see [Experimental Methods](#) and [Supplementary Text 2](#)).

As shown in [Figure 2i–l](#) and [Supplementary Text 4](#), single MEH-PPV chains exhibited decreased fluorescence intensity with a narrowed distribution after SVA. Aggregates B–D emitted much greater fluorescence than single chains, and the fluorescence intensity increased progressively in aggregates B–D. Aggregation led to an attenuation of absorption cross section at the excitation wavelength 488 nm by $\sim 26\%$, requiring a correction constant C_1 to directly compare single molecule and aggregate intensities ([Supplementary Text 5](#)). Following correction for attenuation, the fluorescence intensities of aggregates B–D are ~ 10 , 45, and 165 times higher, respectively, than the single chain intensity. Although fluorescence intensity is not necessarily directly related to aggregate size, these results suggest that the size of conjugated polymer aggregates can be controlled by tuning initial conjugated polymer concentration.

Following fluorescence intensity measurements, excitation polarization modulation depth (M) measurements^{11,26,29–33} were performed for the same imaging areas to assess morphological order of single MEH-PPV chains and aggregates. As shown in [Figure 2m](#), single MEH-PPV chains prepared from dissolution in toluene exhibited high modulation depth, in accordance with previous results,^{26,31–33} suggesting that these single MEH-PPV chains have adopted highly ordered collapsed conformations. The M distribution shifted up after SVA, indicating a further increase in the degree of conformational

order, also consistent with previous results.³³ This M increase upon SVA accompanied decreasing fluorescence intensity of single chains, as noted above. This anticorrelation is discussed in [Supplementary Text 4](#). In the M measurements of aggregates, illumination intensity was carefully adjusted such that potential influence of signal from single chains coexisting with the aggregate under assessment within the diffraction limited feature size was suppressed ([Supplementary Text 6](#)). As shown in [Figure 2n–p](#), the M histograms of all aggregates were centered at high values, indicating that the high degree of morphological order seen in single chains was preserved in the aggregates.

Average Number of Single Chains per Aggregate. The single chain number density in an aggregate, N_{SM-AGG} , can be calculated by $N_{SM-AGG} = (N_{SM,B} - N_{SM,A})/N_{AGG}$. Here, $N_{SM,B}$ and $N_{SM,A}$ are the number of single chains within the full imaging area before and after SVA, respectively, and N_{AGG} is the number of aggregates within the imaging area. Because of the abundance of single chains in films of concentrations B–D and the resultant homogeneous fluorescence observed across the film, a conventional feature counting approach could not be applied. Hence, we formulated analysis appropriate for more concentrated films, with multiple features per diffraction limited spot.

For as-cast films of concentrations B–D, $N_{SM,B}$ within an imaging area could be calculated by dividing the total intensity of the fluorescence image ($I_{film,B}$) by the median fluorescence intensity of a single chain before SVA ($I_{SM,B}$; black in [Figure 2i](#)). The former intensity ($I_{film,B}$) is calculated by summing intensities of every pixel in the fluorescence image. Since annealed films B–D consist of aggregates as well as remaining single chains, the sum of fluorescence intensities from aggregates within an imaging area ($\sum I_{AGG}$) must be subtracted from the total intensity of the fluorescence image ($I_{film,A}$) to obtain the total fluorescence intensity from single chains remaining after SVA. This intensity was then divided by $I_{SM,B}$ corrected for SVA-mediated conformational changes, which is equivalent to $I_{SM,A}$ (gray in [Figure 2i](#)), to calculate $N_{SM,A}$. N_{AGG} is obtained from direct counting from the fluorescence images. The procedure is formulated as

$$N_{SM-AGG} = \frac{\frac{1}{I_{SM,B}} \left\{ I_{film,B} - \frac{1}{C_2} (I_{film,A} - \sum_1^{N_{AGG}} I_{AGG}) \right\}}{N_{AGG}} \quad (2)$$

with C_2 correcting for the decreased fluorescence intensity of single MEH-PPV chains caused by SVA-mediated conformational changes. The correction constant was determined to be 0.83 for single chains present at high density, such as those in as-cast films of concentrations C and D ([Supplementary Text 7](#)). Schematic illustration describing [eq 2](#) and average results and standard deviations for the variables in this equation are provided in [Supplementary Text 8](#). These calculations revealed the number of single molecules in aggregates B–D to be $N_{SM-AGG} \approx 40, 170, \text{ and } 955$, respectively.

Estimation of Physical Size of Mesoscopic Aggregates. Since aggregates B–D were demonstrated to have a high degree of absorption transition dipole alignment as reflected by polarization modulation measurements, we assume the physical structure is also anisotropic and approximate the aggregate shape as a prolate ellipsoid with aspect ratio $\alpha = a/b$, where a and b are the semimajor and semiminor axes,

respectively (inset, [Figure 3](#)). The physical size of the aggregates can be calculated from N_{SM-AGG} via

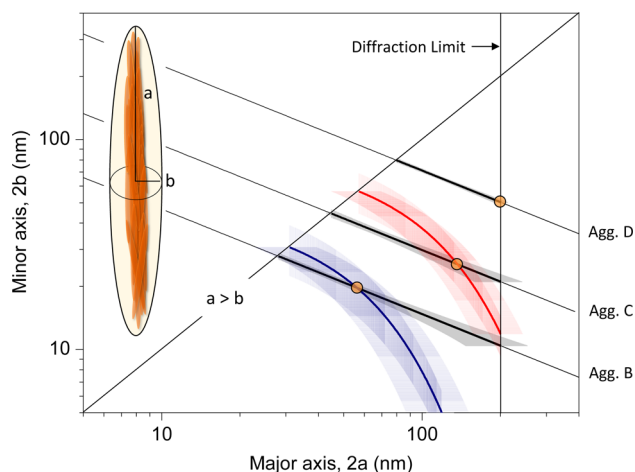


Figure 3. Estimation of physical size of mesoscopic aggregates. Inset shows schematic illustration of aggregate shape; a prolate ellipsoid with a and b the semimajor and semiminor axes, respectively. Thick black lines represent feasible values of $(2a, 2b)$ for aggregates B–D, calculated from N_{SM-AGG} ([eq 3](#)). Blue and red curves represent feasible values of $(2a, 2b)$ for aggregates B and C, respectively, obtained from comparison with diffusion coefficients of aggregates B–D ([eq S6](#)). The uncertainty shown in light colors was calculated using propagation of error from N_{SM-AGG} and D . Yellow dots show determined average physical sizes of the aggregates.

$$\varphi V_{vdW} N_{monomer} N_{SM-AGG} = \frac{4}{3} \pi a b^2 \quad (3)$$

where φ is the packing density of polymer chains, V_{vdW} is the van der Waals volume of the MEH-PPV monomer, and $N_{monomer}$ is the number of monomers in single polymer. We employed $\varphi = 1.52$, the arithmetic mean of the packing densities of crystalline and amorphous MEH-PPV.³⁴ V_{vdW} was calculated to be 0.28 nm^3 and $N_{monomer}$ is 646 for MEH-PPV molecules with $M_w = 168 \text{ kDa}$. Thus, for aggregate D with $N_{SM-AGG} \approx 955$, aggregate volume is calculated to be $\sim 2.7 \times 10^5 \text{ nm}^3$, which in turn is consistent with a series of combinations of $2a$ and $2b$, indicated by a diagonal line in [Figure 3](#).

[Figure 3](#) depicts feasible combinations of $2a$ and $2b$ for aggregates B–D. Here, the lower limit of $2a$ is defined by the boundary condition for a prolate ellipsoid, $a > b$, whereas the upper limit is set by the resolution of the imaging system used here, determined empirically ([Supplementary Text 9](#)). In the images of the annealed films of concentration D, some fluorescent features larger than the diffraction limit were seen. The number of these features increased sharply when film swelling continued slightly longer than 50 min. From these observations, we conclude that aggregate D is, in one dimension, close in size to the diffraction limit. Consequently, of the feasible combinations of $2a$ and $2b$ for aggregate D, we assume its major axis is set by the upper limit of $2a$ in [Figure 3](#). Then, the physical size of the aggregate D is determined to be $2a \approx 200 \text{ nm}$ and $2b \approx 50 \text{ nm}$, with $\alpha \approx 4$.

In parallel with the N_{SM-AGG} -based approach, we assessed aggregate size through measured diffusivity. Since the extent of film swelling during SVA was consistent across experiments ([Figure 1a](#)), aggregates B–D exist in identical viscoelastic

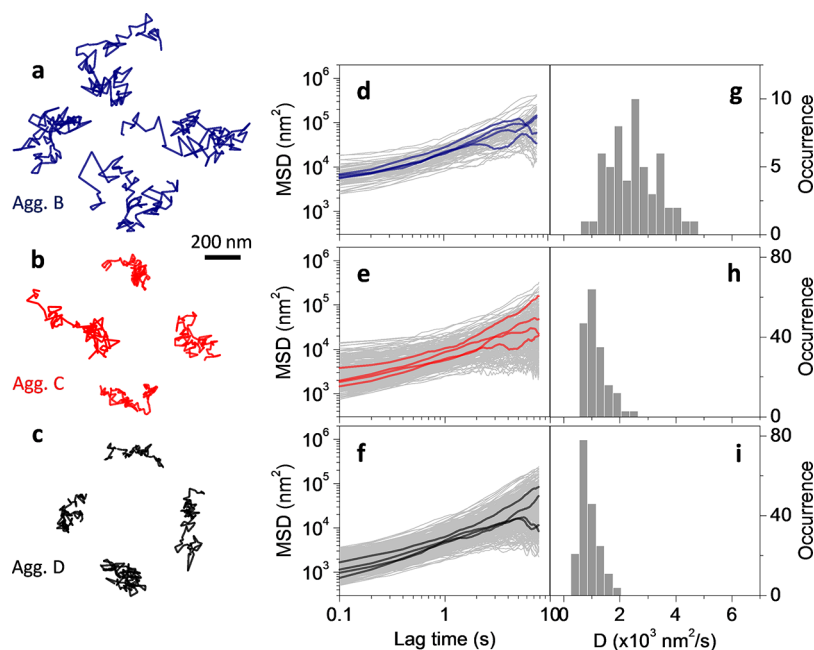


Figure 4. Aggregate diffusion in fully swollen films. (a–c) Typical trajectories of aggregates B–D. Corresponding movies showing diffusing aggregates are provided in [Supplementary Movies S5–7](#). Scale bar is 200 nm. (d–f) MSDs for all aggregates B–D with trajectories longer than 80 consecutive frames. MSDs for the trajectories shown in panels a–c are highlighted in color. (g–i) Histograms of diffusion coefficient, *D*.

environments when the films are swollen to plateau thickness. Thus, the diffusivity of the aggregates can be directly compared.

To assess diffusivity, movies were recorded directly before film deswelling. These movies were recorded under the flow of solvent vapor to maintain the films in their fully swollen state, but diffusing aggregates did not exhibit flow-assisted motion ([Supplementary Text 10](#)). [Figure 4](#) shows typical 2D trajectories for aggregates, MSDs for all analyzed trajectories, and corresponding diffusion coefficient (*D*) histograms. The diffusion coefficient, *D*, was calculated via $\langle \Delta r^2(\tau) \rangle = 2dD\tau + \epsilon$, with *d* the dimensionality of diffusion. Due to the localization uncertainty caused by the low signal-to-background ratio (SBR 1.5–2.0), the offset ϵ was introduced in the fitting procedure. The use of ϵ for fitting data with low SBRs was validated in a previous study³⁵ and from single aggregate trajectory simulations ([Supplementary Text 11](#) and [Movie S4](#)). The median *D* values were 2.53×10^{-11} , 1.05×10^{-11} , and 0.83×10^{-11} cm²/s, respectively, for aggregates B–D.

A relative comparison of *D* of the aggregates yields *a* for aggregates B and C as a function of α (see [Supplementary Text 12](#)), and the resulting combinations of *2a* and *2b* for these aggregates are depicted in [Figure 3](#) (blue and red lines). The size of aggregates B and C is determined to be that consistent with both the estimated volume calculated from N_{SM-AGG} and *D* from experiments. This yields $2a \approx 55$ nm and $2b \approx 20$ nm for aggregate B and $2a \approx 135$ nm and $2b \approx 25$ nm for aggregate C. Single molecule high resolution imaging with photobleaching (SHRImP) analysis³⁶ of the aggregates demonstrated that two emitting positions within a single aggregate C are separated by up to ~ 130 nm, consistent with the physical sizes of the aggregates determined here ([Supplementary Text 13](#)).

Photophysical Characteristics of Morphologically Anisotropic Aggregates. As the single chain number density is known for aggregates B–D, average fluorescence quenching efficiency (QE_{FL}) of these aggregates can be calculated by considering the aggregate fluorescence intensity compared to

that expected from an equal number of single MEH-PPV chains. This can be expressed as

$$QE_{FL} = 1 - \frac{\frac{1}{C_1} \sum_1^{N_{AGG}} I_{AGG}}{N_{AGG} I_{SM,A} N_{SM-AGG}} \quad (4)$$

where C_1 corrects for decreased absorption cross section in aggregates relative to single chains, as described above and in [Supplementary Text 5](#). Strikingly, aggregation of MEH-PPV molecules caused very strong fluorescence quenching: $\sim 68\%$, 77% , and 88% , respectively, for aggregates B–D. While aggregation initially results in a significant loss of fluorescence, as seen in aggregate B, the degree of fluorescence quenching has a relatively weak dependence on aggregate size. The observed QE_{FL} for aggregates B–D is consistent with the high degree of quenching found in bulk solution and film studies and is likely attributable primarily to the formation of interchain species such as polaron pairs,^{19,37} excimers,^{38,39} and H-aggregates.^{40,41} This observation, however, contradicts a previous report,¹¹ where little quenching was observed for the MEH-PPV aggregates prepared, regardless of aggregate size and degree of morphological ordering. Assuming interchain species are the primary source of fluorescence quenching in MEH-PPV aggregates, this disparity may be related to differences in structure and density of chain packing within aggregates that may arise from differences in MEH-PPV molecular weight, differences in SVA processing conditions, or differences in methods assessing the number of single chains in an aggregate.

While quenching in aggregates is significant, overall fluorescence intensity of MEH-PPV aggregates is strong, suggesting the presence of many excitons surviving fast quenching processes. To characterize diffusion of these excitons, we performed fluorescence intensity transient measurements. Aggregates B and C, as well as single MEH-PPV chains, predominantly exhibited stepwise photobleaching

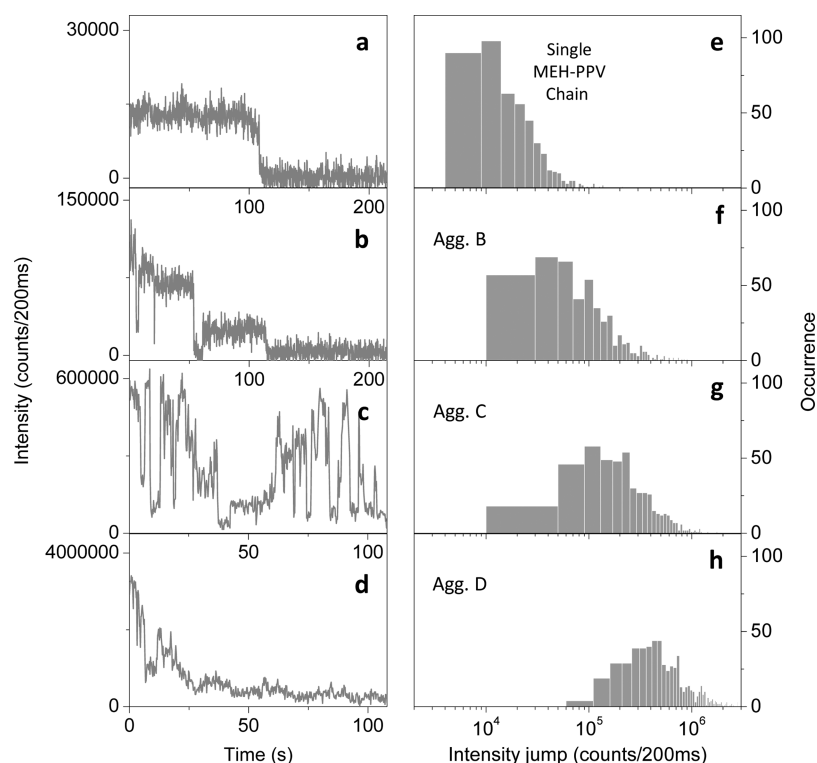


Figure 5. Photobleaching characteristics of morphologically anisotropic aggregates. (a–d) Representative fluorescence intensity transients of single MEH-PPV molecules after SVA and aggregates B–D. (e–h) Histograms of fluorescence intensity jump size between neighboring intensity levels obtained from assessment of the initial three stepwise transitions in fluorescence intensity transients; 500 transitions were analyzed for each histogram. Median jump sizes are 15800, 92700, 234300, and 536500 counts per 200 ms, respectively, for single chains after SVA and aggregates B–D.

and fluorescence blinking behaviors (Figure 5a–c), similar to single MEH-PPV molecules in ordered conformations and distinct from the continuous photobleaching behavior seen in those with random coil conformation.^{36,42–44} Aggregate D also exhibited these behaviors until fluorescence decreased to approximately half the initial intensity, after which fluorescence decay appeared quasicontinuous (Figure 5d). Since aggregate D consists of nominally >30 000 chromophores,^{45,46} the observed discrete fluorescence transitions must result from efficient exciton transport within the aggregates.^{36,42–44} Surprisingly, some of the aggregates B and C exhibited complete fluorescence intermittency, indicating that these mesoscopic entities behave as single quantum systems.

To explore dependence of exciton diffusion characteristics on aggregate size, we assessed fluorescence intensity jump size between neighboring intensity levels in the fluorescence intensity transients of single MEH-PPV chains and aggregates B–D. Discrete intensity levels were identified using a step transition and state identification algorithm (see [Experimental Methods](#)), and representative results of this procedure are shown in [Supplementary Text 14](#). For the initial four intensity levels, the jump size between neighboring intensity levels is a factor of ~6 times greater in aggregate B than in single MEH-PPV chains (Figure 5e,f). The jump size continued to increase from aggregates B to D (Figure 5f–h). The increasing fluorescence intensity jump size implies that the size of exciton domains, largely independent spatial regions in which exciton transfer occurs to a single trapping site, becomes larger with the physical size of the aggregates. This reveals a strong mesoscale correlation between length scale of exciton transport and physical size in conjugated polymer aggregates.

Growth of Conjugated Polymer Fiber Aggregates and 2D Fiber Networks.

Given that initial polymer concentration correlated strongly with aggregate size in the employed SVA protocol, we attempted to grow even larger aggregates by preparing a sample film with an initial MEH-PPV concentration 10 times higher than concentration D. SVA of this film led to the growth of morphologically anisotropic MEH-PPV fibers with characteristic length well beyond the diffraction limit. As shown in [Figure 6a–c](#), while the widths of these fiber aggregates did not exceed the diffraction limit, their lengths were typically 1–5 μm . Short fiber aggregates were largely linear. Increasing fiber length was accompanied by emergence of structural heterogeneity, with longer fiber aggregates exhibiting bends or kinks as well as branching. These structural

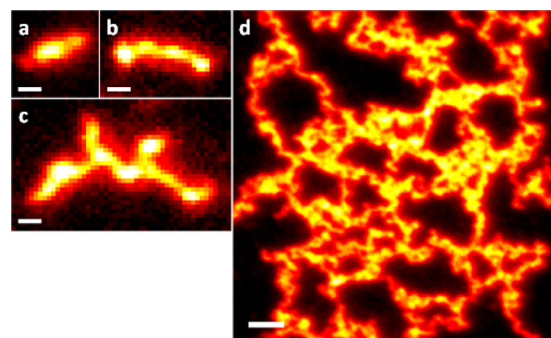


Figure 6. Preparation of microscopic aggregates. Fluorescence images of (a–c) MEH-PPV fiber aggregates and (d) a network thereof. Scale bars in panels a–c and d are 0.5 and 2 μm , respectively.

characteristics were dynamic: when in the swollen film, fiber aggregates exhibited apparent changes in structure, such as degree of bending, over time (Supplementary Text 15 and Movie S8).

Strikingly, SVA of a sample film with initial MEH-PPV concentration of ~ 30 nM (~ 100 times concentration D) for 20 h led to the formation of a fiber network (Figure 6d). In accordance with recent reports that such structures, despite the presence of disorder, facilitate transport of charge carriers along ordered regions,^{1–3} such an interconnected network holds promise for long-range charge transport. The fiber networks prepared here are similar morphologically to those present in bulk heterojunction active layers of polymer-based devices;^{3,9} however, the characteristic length scale here is at least an order of magnitude greater.

CONCLUSIONS

Despite early success characterizing and directing MEH-PPV conformation on a single molecule level, controlling mesoscopic morphological order of conjugated polymer aggregates is difficult, as the structure and properties of aggregates rely on supramolecular chemistry and, in turn, on the processing conditions under which they are prepared. We demonstrated that aggregate size and morphology can be controlled from the mesoscopic to microstructural scales. Further, we developed analyses that allow quantitative assessment of fundamental aggregate attributes associated with device performance. In particular, intensity analysis of concentrated films combined with diffusion analysis of individual aggregates allowed for determination of single chain number density and physical size as well as degree of photoluminescence quenching in mesoscale aggregates. These aggregates exhibited discrete changes in intensity, with extent of changes increasing with physical size, demonstrating efficient exciton diffusion at the mesoscopic length scale.

On the longest length scales explored, the formation of micrometer-scale fiber aggregates directly demonstrates that single molecule anisotropy morphology is preserved even at the microstructural scale. This structural anisotropy may facilitate directional, long-range exciton diffusion along the fiber backbone, as seen recently in 1D H-aggregated nanofibers.⁴⁷ Moreover, interconnected networks of fiber aggregates prepared here resemble the morphology of active layers in bulk heterojunction devices and may allow device-scale transport of charge carriers.

ASSOCIATED CONTENT

Supporting Information

The Supporting Information is available free of charge on the ACS Publications website at DOI: 10.1021/acs.jpcc.7b02257.

- (1) Determination of film thickness, (2) size and shape of fluorescent features, (3) pixel intensity distributions of fluorescence images, (4) fluorescence intensity and polarization anisotropy of single MEH-PPV chains, (5) change of absorption cross section upon aggregation, (6) polarization modulation depth of aggregates, (7) SVA-induced conformational changes of single MEH-PPV chains present at high density, (8) number of single molecules per aggregate and quenching efficiency for aggregates, (9) empirical lateral resolution of the imaging system, (10) trajectory angle of single aggregate motion, (11) single aggregate trajectory simulations, (12) relative

- diffusion coefficients of aggregates, (13) single aggregate high resolution imaging with photobleaching, (14) fluorescence intensity state identification, and (15) wriggling of a fiber aggregate in a swollen film (PDF)
- Aggregation during SVA, recorded 10 min after start of SVA (AVI)
- Aggregation during SVA, recorded 20 min after start of SVA (AVI)
- Aggregation during SVA, recorded 47 min after start of SVA (AVI)
- Simulation of single aggregate diffusion (AVI)
- Tracked motion of individual aggregates B (AVI)
- Tracked motion of individual aggregates C (AVI)
- Tracked motion of individual aggregates D (AVI)
- Wriggling of a fiber aggregate in a swollen film (AVI)

AUTHOR INFORMATION

Corresponding Author

*E-mail: kaufman@chem.columbia.edu.

ORCID

Laura J. Kaufman: 0000-0002-3754-0831

Present Address

[†]H.P.: Department of Physics, Texas A&M University, Commerce, TX 75428.

Notes

The authors declare no competing financial interest.

ACKNOWLEDGMENTS

This work was supported in part by the National Science Foundation under grant CHE1213242. The authors are grateful to Prof. Daniel A. Higgins for sharing Igor code and Dat Hoang and Khanh-Hoa Tran-Ba for assistance in simulations and aggregate tracking.

REFERENCES

- (1) Noriega, R.; Rivnay, J.; Vandewal, K.; Koch, F. P. V.; Stingelin, N.; Smith, P.; Toney, M. F.; Salleo, A. A General Relationship between Disorder, Aggregation and Charge Transport in Conjugated Polymers. *Nat. Mater.* **2013**, *12*, 1038–1044.
- (2) Jackson, N. E.; Kohlstedt, K. L.; Savoie, B. M.; Olvera de la Cruz, M.; Schatz, G. C.; Chen, L. X.; Ratner, M. A. Conformational Order in Aggregates of Conjugated Polymers. *J. Am. Chem. Soc.* **2015**, *137*, 6254–6262.
- (3) Wang, D.; Liu, F.; Yagihashi, N.; Nakaya, M.; Ferdous, S.; Liang, X. B.; Muramatsu, A.; Nakajima, K.; Russell, T. P. New Insights into Morphology of High Performance Bhj Photovoltaics Revealed by High Resolution Afm. *Nano Lett.* **2014**, *14*, 5727–5732.
- (4) He, Z. C.; Zhong, C. M.; Su, S. J.; Xu, M.; Wu, H. B.; Cao, Y. Enhanced Power-Conversion Efficiency in Polymer Solar Cells Using an Inverted Device Structure. *Nat. Photonics* **2012**, *6*, 593–597.
- (5) Chen, H. J.; Guo, Y. L.; Yu, G.; Zhao, Y.; Zhang, J.; Gao, D.; Liu, H. T.; Liu, Y. Q. Highly P-Extended Copolymers with Diketopyrrolopyrrole Moieties for High-Performance Field-Effect Transistors. *Adv. Mater.* **2012**, *24*, 4618–4622.
- (6) Facchetti, A. Pi-Conjugated Polymers for Organic Electronics and Photovoltaic Cell Applications. *Chem. Mater.* **2011**, *23*, 733–758.
- (7) Zhang, W. M.; et al. Indacenodithiophene Semiconducting Polymers for High-Performance, Air-Stable Transistors. *J. Am. Chem. Soc.* **2010**, *132*, 11437–11439.
- (8) Barbara, P. F.; Gesquiere, A. J.; Park, S. J.; Lee, Y. J. Single-Molecule Spectroscopy of Conjugated Polymers. *Acc. Chem. Res.* **2005**, *38*, 602–10.
- (9) van Franeker, J. J.; Heintges, G. H. L.; Schaefer, C.; Portale, G.; Li, W. W.; Wienk, M. M.; van der Schoot, P.; Janssen, R. A. J. Polymer

Solar Cells: Solubility Controls Fiber Network Formation. *J. Am. Chem. Soc.* **2015**, *137*, 11783–11794.

(10) Hedley, G. J.; Ward, A. J.; Alekseev, A.; Howells, C. T.; Martins, E. R.; Serrano, L. A.; Cooke, G.; Ruseckas, A.; Samuel, I. D. W. Determining the Optimum Morphology in High-Performance Polymer-Fullerene Organic Photovoltaic Cells. *Nat. Commun.* **2013**, *4*, 2867.

(11) Vogelsang, J.; Adachi, T.; Brazard, J.; Vanden Bout, D. A.; Barbara, P. F. Self-Assembly of Highly Ordered Conjugated Polymer Aggregates with Long-Range Energy Transfer. *Nat. Mater.* **2011**, *10*, 942–946.

(12) Traub, M. C.; Vogelsang, J.; Plunkett, K. N.; Nuckolls, C.; Barbara, P. F.; Vanden Bout, D. A. Unmasking Bulk Exciton Traps and Interchain Electronic Interactions with Single Conjugated Polymer Aggregates. *ACS Nano* **2012**, *6*, 523–529.

(13) Hu, Z. J.; Adachi, T.; Haws, R.; Shuang, B.; Ono, R. J.; Bielawski, C. W.; Landes, C. F.; Rossky, P. J.; Vanden Bout, D. A. Excitonic Energy Migration in Conjugated Polymers: The Critical Role of Interchain Morphology. *J. Am. Chem. Soc.* **2014**, *136*, 16023–16031.

(14) Stangl, T.; Wilhelm, P.; Remmersen, K.; Hoger, S.; Vogelsang, J.; Lupton, J. M. Mesoscopic Quantum Emitters from Deterministic Aggregates of Conjugated Polymers. *Proc. Natl. Acad. Sci. U. S. A.* **2015**, *112*, E5560–E5566.

(15) Szymanski, C.; Wu, C. F.; Hooper, J.; Salazar, M. A.; Perdomo, A.; Dukes, A.; McNeill, J. Single Molecule Nanoparticles of the Conjugated Polymer Meh-Ppv, Preparation and Characterization by near-Field Scanning Optical Microscopy. *J. Phys. Chem. B* **2005**, *109*, 8543–8546.

(16) Grey, J. K.; Kim, D. Y.; Norris, B. C.; Miller, W. L.; Barbara, P. F. Size-Dependent Spectroscopic Properties of Conjugated Polymer Nanoparticles. *J. Phys. Chem. B* **2006**, *110*, 25568–25572.

(17) Lin, H. Z.; Hania, R. P.; Bloem, R.; Mirzov, O.; Thomsson, D.; Scheblykin, I. G. Single Chain Versus Single Aggregate Spectroscopy of Conjugated Polymers. Where Is the Border? *Phys. Chem. Chem. Phys.* **2010**, *12*, 11770–11777.

(18) Nguyen, T. Q.; Doan, V.; Schwartz, B. J. Conjugated Polymer Aggregates in Solution: Control of Interchain Interactions. *J. Chem. Phys.* **1999**, *110*, 4068–4078.

(19) Wang, P.; Collison, C. J.; Rothberg, L. J. Origins of Aggregation Quenching in Luminescent Phenylenevinylene Polymers. *J. Photochem. Photobiol., A* **2001**, *144*, 63–68.

(20) Gotrik, K. W.; Hannon, A. F.; Son, J. G.; Keller, B.; Alexander-Katz, A.; Ross, C. A. Morphology Control in Block Copolymer Films Using Mixed Solvent Vapors. *ACS Nano* **2012**, *6*, 8052–8059.

(21) Sinturel, C.; Vayer, M.; Morris, M.; Hillmyer, M. A. Solvent Vapor Annealing of Block Polymer Thin Films. *Macromolecules* **2013**, *46*, 5399–5415.

(22) Hoang, D. T.; Yang, J.; Paeng, K.; Kwon, Y.; Kweon, O. S.; Kaufman, L. J. In Situ Multi-Modal Monitoring of Solvent Vapor Swelling in Polymer Thin Films. *Rev. Sci. Instrum.* **2016**, *87*, 015106.

(23) Neef, C. J.; Ferraris, J. P. Meh-Ppv: Improved Synthetic Procedure and Molecular Weight Control. *Macromolecules* **2000**, *33*, 2311–2314.

(24) Sahoo, D.; Tian, Y. X.; Sforzini, G.; Anderson, H. L.; Scheblykin, I. G. Photo-Induced Fluorescence Quenching in Conjugated Polymers Dispersed in Solid Matrices at Low Concentration. *J. Mater. Chem. C* **2014**, *2*, 6601–6608.

(25) Crocker, J. C.; Grier, D. G. Methods of Digital Video Microscopy for Colloidal Studies. *J. Colloid Interface Sci.* **1996**, *179*, 298–310.

(26) Park, H.; Hoang, D. T.; Paeng, K.; Yang, J.; Kaufman, L. J. Conformation-Dependent Photostability among and within Single Conjugated Polymers. *Nano Lett.* **2015**, *15*, 7604–7609.

(27) Shuang, B.; Cooper, D.; Taylor, J. N.; Kisley, L.; Chen, J. X.; Wang, W. X.; Li, C. B.; Komatsuzaki, T.; Landes, C. F. Fast Step Transition and State Identification (Stasi) for Discrete Single-Molecule Data Analysis. *J. Phys. Chem. Lett.* **2014**, *5*, 3157–3161.

(28) Levin, A.; et al. Ostwald's Rule of Stages Governs Structural Transitions and Morphology of Dipeptide Supramolecular Polymers. *Nat. Commun.* **2014**, *5*, 5219.

(29) Hu, D. H.; Yu, J.; Wong, K.; Bagchi, B.; Rossky, P. J.; Barbara, P. F. Collapse of Stiff Conjugated Polymers with Chemical Defects into Ordered, Cylindrical Conformations. *Nature* **2000**, *405*, 1030–1033.

(30) Furumaki, S.; Habuchi, S.; Vacha, M. Fluorescence-Detected Three-Dimensional Linear Dichroism: A Method to Determine Absorption Anisotropy in Single Sub-Wavelength Size Nanoparticles. *Chem. Phys. Lett.* **2010**, *487*, 312–314.

(31) Mirzov, O.; Bloem, R.; Hania, P. R.; Thomsson, D.; Lin, H. Z.; Scheblykin, I. G. Polarization Portraits of Single Multichromophoric Systems: Visualizing Conformation and Energy Transfer. *Small* **2009**, *5*, 1877–1888.

(32) Adachi, T.; Brazard, J.; Chokshi, P.; Bolinger, J. C.; Ganesan, V.; Barbara, P. F. Highly Ordered Single Conjugated Polymer Chain Rod Morphologies. *J. Phys. Chem. C* **2010**, *114*, 20896–20902.

(33) Vogelsang, J.; Brazard, J.; Adachi, T.; Bolinger, J. C.; Barbara, P. F. Watching the Annealing Process One Polymer Chain at a Time. *Angew. Chem., Int. Ed.* **2011**, *50*, 2257–2261.

(34) Krevelen, D. W. V.; Nijenhuis, K. T. *Properties of Polymers*, 4th ed.; Elsevier: Amsterdam, 2009.

(35) Michalet, X. Mean Square Displacement Analysis of Single-Particle Trajectories with Localization Error: Brownian Motion in an Isotropic Medium. *Phys. Rev. E* **2010**, *82*, 041914.

(36) Park, H.; Hoang, D. T.; Paeng, K.; Kaufman, L. J. Localizing Exciton Recombination Sites in Conformationally Distinct Single Conjugated Polymers by Super-Resolution Fluorescence Imaging. *ACS Nano* **2015**, *9*, 3151–3158.

(37) Yan, M.; Rothberg, L. J.; Papadimitrakopoulos, F.; Galvin, M. E.; Miller, T. M. Spatially Indirect Excitons as Primary Photoexcitations in Conjugated Polymers. *Phys. Rev. Lett.* **1994**, *72*, 1104–1107.

(38) Jakubiak, R.; Collison, C. J.; Wan, W. C.; Rothberg, L. J.; Hsieh, B. R. Aggregation Quenching of Luminescence in Electroluminescent Conjugated Polymers. *J. Phys. Chem. A* **1999**, *103*, 2394–2398.

(39) Samuel, I. D. W.; Rumbles, G.; Collison, C. J. Efficient Interchain Photoluminescence in a High-Electron-Affinity Conjugated Polymer. *Phys. Rev. B: Condens. Matter Mater. Phys.* **1995**, *52*, R11573–R11576.

(40) Spano, F. C.; Silva, C. H. and J-Aggregate Behavior in Polymeric Semiconductors. *Annu. Rev. Phys. Chem.* **2014**, *65*, 477–500.

(41) Chakraborty, R.; Rothberg, L. J. Role of Aggregates in the Luminescence Decay Dynamics of Conjugated Polymers. *J. Phys. Chem. A* **2016**, *120*, 551–555.

(42) Huser, T.; Yan, M.; Rothberg, L. J. Single Chain Spectroscopy of Conformational Dependence of Conjugated Polymer Photophysics. *Proc. Natl. Acad. Sci. U. S. A.* **2000**, *97*, 11187–11191.

(43) Sarzi Sartori, S.; De Feyter, S.; Hofkens, J.; Van der Auweraer, M.; De Schryver, F.; Brunner, K.; Hofstraat, J. W. Host Matrix Dependence on the Photophysical Properties of Individual Conjugated Polymer Chains. *Macromolecules* **2003**, *36*, 500–507.

(44) Ebihara, Y.; Vacha, M. Relating Conformation and Photophysics in Single Meh-Ppv Chains. *J. Phys. Chem. B* **2008**, *112*, 12575–12578.

(45) DuBay, K. H.; Hall, M. L.; Hughes, T. F.; Wu, C.; Reichman, D. R.; Friesner, R. A. Accurate Force Field Development for Modeling Conjugated Polymers. *J. Chem. Theory Comput.* **2012**, *8*, 4556–4569.

(46) Köhler, A.; Hoffmann, S. T.; Bässler, H. An Order–Disorder Transition in the Conjugated Polymer Meh-Ppv. *J. Am. Chem. Soc.* **2012**, *134*, 11594–11601.

(47) Haedler, A. T.; Kreger, K.; Issac, A.; Wittmann, B.; Kivala, M.; Hammer, N.; Kohler, J.; Schmidt, H. W.; Hildner, R. Long-Range Energy Transport in Single Supramolecular Nanofibres at Room Temperature. *Nature* **2015**, *523*, 196–199.